Enzyme-coupled nanoplasmonic biosensing of cancer markers in human serum

Na rae Jo, Ki joong Lee, Yong-Beom Shin

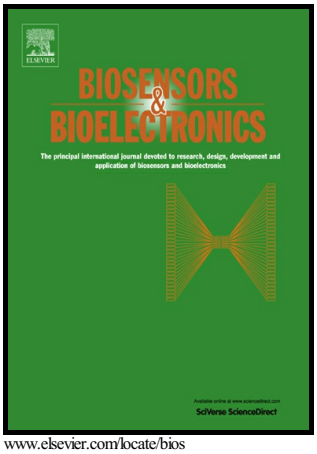

www.elsevier.com/locate/bios

PII: S0956-5663(16)30201-9
DOI: http://dx.doi.org/10.1016/j.bios.2016.03.009
Reference: BIOS8520

To appear in: *Biosensors and Bioelectronic*

Received date: 27 January 2016
Revised date: 3 March 2016
Accepted date: 7 March 2016

Cite this article as: Na rae Jo, Ki joong Lee and Yong-Beom Shin, Enzyme coupled nanoplasmonic biosensing of cancer markers in human serum *Biosensors and Bioelectronic,* http://dx.doi.org/10.1016/j.bios.2016.03.009

Enzyme-coupled nanoplasmonic biosensing of cancer markers in human serum

Na rae Jo[a], Ki joong Lee[b], Yong-Beom Shin[a,b*]

[a]Department of Nanobiotechnology, Korea University of Science and Technology (UST), 305-350, Republic Korea

[b]Hazards Monitoring Bionano Research Center, Korea Research Institute of Bioscience and Biotechnology (KRIBB), 305-806, Republic of Korea

[*]Corresponding author at: Hazards Monitoring Bionano Research Center, Korea Research Institute of Bioscience and Biotechnology (KRIBB), Republic of Korea, and Department of Nanobiotechnology, Korea University of Science and Technology (UST), Republic Korea, Tel.: +82 8604449; Fax: +82 8798596 , Email address: ybshin@kribb.re.kr

Abstract

As the use of biosensors for early *in-vitro* diagnosis of malignant diseases has expanded, issues associated with ultra-sensitivity and wide dynamic range have become paramount. In this study, we designed a sub-zeptomolar sensor for detecting the alpha-feto protein (AFP) that utilizes localized surface plasmon resonance (LSPR) assisted by bio-catalytic reaction and a self-controlled detection scheme. A gold nanodot array (GNA), serving as a plasmonic material, was fabricated using an improved UV nanoimprint lithography (NIL) method that employs a sacrificial layer. In the new approach, LSPR observation is highly stable because it employs a back reflection mode, which avoids passing the signal through the sample solution. An enzyme-precipitation reaction was conducted on the AFP antigen-antibody complex on the surface of the gold nanodot (nano-ELISA) using a procedure that was described previously. To extend the AFP detection limit below femtomolar concentrations, a scheme involving self-controlled detection was employed to lower the limit. In this method, the

sample including the target simultaneously plays the role of both sample and negative control. Using this scheme, AFP can be detected at concentrations as low as 14 aM (0.7 zeptomole in 50 μL serum) and with the wide dynamic range of 10 fg mL^{-1}-10 ng mL^{-1}. Importantly, the new method provides a platform for studying and monitoring interactions between biochemically active substances that are present in very low concentrations. Finally, the general strategy used to design the detection method can be easily adapted to the ultra-sensitive detection of other biomarkers and pathogens.

Keywords: biosensor, localized surface plasmon, UV nanoimprint, enzymatic precipitation reaction, self-controlled

1. Introduction

Owing to the collective oscillation of free electrons that is promoted by the interaction of the incident light of specific energies with 3-dimensional metal nanostructures, intense scattering and light absorption occurs, which are referred to as nanoplasmonic phenomena. The key feature of nanoplasmonic systems is that the distribution of the evanescent field near the surface of the metal nanostructures becomes concentrated in the range from half the penetration depth for a propagating surface plasmon (PSP or surface plasmon polariton; SPP) to a few nanometers, and a resultant enhancement of the electromagnetic field intensity occurs. This feature enables nanoplasmonic technology to serve as a powerful tool for biochemical sensing applications that rely on surface-enhanced Raman (Brown et al., 2013; Geddes et al., 2003; Haynes et al., 2005; Jeanmaire et al., 1977) and fluorescence (Ha et al.,1996; Schultz et al., 2000; Touahir et al. 2010; Yang et al. 2015; Yguerabide et al., 1998) spectroscopic methods. In addition, this feature of nanoplasmonic systems allows them to be

employed in label-free sensing technologies that are based on monitoring changes in the dielectric constant around metal surfaces, generally defined as localized surface plasmon resonance (LSPR) (Endo et al., 2005; Jeong and Lee et al., 2011; Kim et al., 2005; Mock et al., 2003; Nath et al., 2004; Raschke et all., 2003). The LSPR technique has several advantageous features including small sensing volumes, minimal temperature effects and the use of simple optics components, which contrasts with the requirements of PSP (Dahlin et al., 2009; Haes et al., 2004) that is generated in semi-infinitely continuous metal nano-films. In general, an LSP field in an isolated metal nanostructure has a decay length of approximately 30 nm (Yonzon et al., 2005), and, moreover, it is intensively distributed over short distances (<5 nm) from the metal surface (Haes et al., 2002). Therefore, LSPR is very sensitive to changes in close proximity to the surface of metal nanostructures. For this reason, LSPR can be employed for real-time monitoring of biomolecule binding to receptors on the metal surface and, consequently, as a promising tool for biosensing.

Unfortunately, the short penetration depth of the LSP field can be a detriment when large-sized antibodies are utilized as bioreceptors to recognize a specific target molecule such as an antigen (Haes et al., 2003; Jonsson et al.; 2008). Specifically, analyte molecules bound to large receptor molecules immobilized on the surface of a plasmonic metal nanostructure are not readily detected, even if they reside within the LSP field. This phenomenon makes direct detection of targets difficult, especially when they are present in low concentrations. A few reports have described how this limitation can be circumvented by reducing the size of the receptor molecule (Byun et al., 2013; Guo and L et al., 2012; Kim et al., 2009).

Another approach to overcoming this obstacle in LSPR biosensing involves using an enzyme-precipitation reaction on gold nanodots after carrying out the antigen-antibody reaction that

was described in a previous study (Lee et al., 2011). The enzyme reaction derived from enzyme-linked immunosorbent assay (ELISA) produces insoluble precipitates of high dielectric constant that are stacked on the metal surface. This causes a large change in the refractive index within the range of the sensing depth, which leads to a large amplification of the wavelength change in LSPR. However, owing to nonspecific binding and chip-to-chip variations in the nanodot surfaces, it is difficult to employ this technique to decrease the limit of detection (LOD) beyond a few pg mL^{-1}, especially in assays of real biosamples such as those derived from blood and serum.

In the study described below, a new LSPR-based assay system was developed for the ultra-sensitive sensing of biomolecules that relies on the use of a self-controlled detection system. The approach uses enzyme-enhanced LSPR on gold nanodot array (GNA) chips that are easily fabricated using UV nanoimprint lithography. In the self-controlled detection scheme, a separate reference sample as a negative control, which should be prepared to assay an analyte quantitatively in general, is not required. Instead, the sample containing the target analyte simultaneously plays the role of both the target in the sample channel and a negative control in the reference channel. In addition, the assay system employs a back-reflection method, in which nanodots are irradiated with light from the backside of the glass substrate and the emitted light is reflected from the metal nanostructures and transmitted to the detector from the back of the substrate. By using this configuration, the probe light never passes through the sample solution during the measurement, and, as a result, precise and reliable data can be acquired without signal drift originating from the temporary perturbation of sample solutions.

In this investigation, alpha-fetoprotein (AFP) was chosen as the disease marker ~~we employed~~ to demonstrate the highly sensitive nature of the immunosensing system that employs LSPR

and the techniques described above. AFP is a plasma protein (70 kDa) that consists of 591 amino acids, which serve as a clinical marker of tumors such as hepatocellular carcinoma and germ cell tumor (Seppälä et al., 1973). The concentration of AFP in serum is less than 25 ng mL^{-1} in healthy adults (Zhu et al., 2006). AFP has been detected using various biosensor techniques including chemiluminescent immunoassays, electrochemiluminescence and piezoelectric immunosensors (Fu et al., 2006; Guo et al., 2012; Liu et al., 2010; Tsai and Lin., 2005; Wang et al., 2009). In addition, AFP detection based on LSPR coupled fluorescence system has been reported, and its detection limit was 2.33 ng mL^{-1} (Chang et al., 2009). Therefore, the detection of extremely low concentrations of AFP using LSPR-based systems has not been reported to date. Moreover, the existence in serum of many other proteins makes the immuno-detection of limited-abundance targets such as AFP a difficult task. In the current effort described below, a biosensor that utilizes a nanoplasmonic sensor, an ELISA process on gold nanodots (nano-ELISA) and a self-controlled detection scheme, was successfully developed for immunoassay. The new sensing method enables the detection of AFP in human serum with an extremely low LOD.

2. Material and methods

2.1 Material

11-Mercaptoundecanoic acid (MUA), 1-ethyl-3-(3-dimethylaminopropyl)-carbodiimide, N-hydroxysuccinimide, bovine serum albumin (BSA), 5-bromo-4-chloro-3-indolyl phosphate p-toluidine, streptavidin-alkaline phosphatase, poly (butyl methacrylate-co-methyl methacrylate), tetramethylammonium hydroxide (TMAH) solution and nitro blue tetrazolium were purchased from Sigma. Recombinant AFP, anti-AFP antibody and biotinylated anti-AFP antibody were obtained from Meridian Life Science. AFP Affinity Stripped Human serum

was purchased from Cone Products. In its total protein >5.0 mIU mL^{-1}, the analytes include calcium <10 mg dL^{-1}, sodium 130-148 mmol L^{-1} and so on at pH 7.0-7.4 with bioburden < 10cfu mL^{-1}. An AFP ELISA kit (ALPHADIAGNOSTIC Intl.) was used for a comparative test. An imprint resin, NIPSC28LV400, and a UV-curable perfluoropolyether (PFPE) for replication of a master were purchased from Chemoptics and Solvay Solexis, repectively.

2.2 Fabrication of the GNA chip

The GNA chip fabrication was carried out in consecutive procedures. Nanoimprint lithography was facilitated to construct the gold nanodot arrays on a glass substrate. First, silicon masters patterned with a hexagonal hole array with a diameter of 150 nm, a depth of 150 nm and a period of 300 nm were fabricated by deep ultraviolet lithography (ASML, PAS5500/700D KrF Scanner, 248 nm) and etched by deep reactive ion etching (LAM, TCP-9400DFM). UV-curable perfluoropolyether (PFPE, MD700) was coated on the silicon master, and polycarbonate (PC) film was pressed with a hand-roller to fill the hole patterns with the UV resin. Then, the resin was cured with UV (365 nm) at an intensity of 1 kW cm^{-2} for 180 sec. The PC film patterned with PFPE nanopillar was stripped from the master, and then the surface of the nanopillar was modified for easy demolding. Poly (butyl methacrylate-co-methyl methacrylate) as a sacrificial layer was deposited on the glass wafer at 4000 rpm for 30 sec. After the sacrificial layer was baked on a hot plate at 120 °C for 2 min, NIPSC28LV400 was coated on the sacrificial layer. The imprinting was performed with UV illumination (365 nm) under the pressure of 5 bar for 180 sec. To protect the top area of pillar-shaped resin from O_2 plasma etching, a 30 nm layer of chromium was deposited at a tilted angle of 70° during rotation in an e-beam evaporator. The residual layer was removed by O_2 plasma etching (PINK Gmbh plasma-finish) at an O_2 flow rate of 300 mL min^{-1} and

300 W for 40 min. Finally, a Ti/Au layer (1 nm/20 nm) was deposited by e-beam evaporation, and lift-off was achieved with 25% TMAH solution at 90 °C for 15 min. The fabrication process is briefly described in Fig. 1a.

2.3 Modification and functionalization of the GNA chip for AFP detection

The GNA chips was cleaned with piranha solution (H_2SO_4/H_2O_2 = 3:1) at 120 ℃ to eliminate the impurities on the surface of the chips; then, they were rinsed with deionized water (DW) and dried with nitrogen gas. The cleaned chips were bathed in 10 mM 11-mercaptoundecanoic acid (MUA) solution for 12 h. The carboxylate groups of the MUA surfaces were activated in a solution of 0.1 M of 1-ethyl-3-(3-dimethylaminopropyl)-carbodiimide and 0.025 M of N-hydroxysuccinimide in DW for 15 min. 0.1 mg mL^{-1} anti-AFP antibody in PBS was injected and incubated for 30 min. To prevent nonspecific binding, 10mg mL^{-1} bovine serum albumin (BSA) was applied and incubated for 30 min. Recombinant AFP at various concentrations (1 fg mL^{-1} - 100 ng mL^{-1}) in human serum was injected and then incubated for 30 min for the antibody-antigen interaction. The sandwich immunoassay was performed for 30 min with biotinylated anti-AFP antibody of 1 μg mL^{-1} and 1 μg mL^{-1} of streptavidin-alkaline phosphatase in a PBS solution containing 1 mg mL^{-1} BSA. The enzyme-catalyzed precipitation reaction was triggered by adding 0.1 M 5-bromo-4-chloro-3-indolyl phosphate p-toluidine and 1 mg mL^{-1} nitro blue tetrazolium in an AP buffer (100 mM Tris-HCl, 100 mM NaCl, 5 mM $MgCl_2$) at pH 9.5 for 30 min. All sample volumes were 50 μL.

2.4 Back-reflection configuration for LSPR measurement

In our LSPR observation setup with the back-reflection mode, a bundle-typed reflection/backscatter probe (OceanOptics) was used, in which the probe light from a white light source (Carl Zeiss) was vertically delivered to the GNA along the branch of the light-inlet through the backside of the glass substrate and then the reflected light from the GNA propagated to a potable spectrometer (OceanOptics) along the outlet branch of the bundle optical fiber (Fig. S1 in the Supplementary information). In every process, the LSP spectrum was measured in real time at a data acquisition rate of 0.33 Hz, and LSPR wavelength was determined by the centroid fit using a homemade program based on LabVIEW.

2.5 Numerical simulation

The theoretical calculation was performed with FDTD Solutions (Lumerical Inc.). To calculate the plasmonic regions on the gold nanodots, a used planar electromagnetic wave was propagated in z direction normal to the backside surface of the glass substrate and was in polarization along the x-axis with wavelengths ranging from 600 to 1100 nm. Then, the light went into a box-shaped space containing a nanodot to simulate the interaction between the propagating plane wave and a gold nanodot. The boundaries of the simulation region were assigned periodic boundary conditions. The refractive index of the top and side media was chosen as 1.3329 (DW), and that of the substrate (glass) medium was set to 1.52. An analytic form of the material with Drude and Lorentzian terms was used, ensuring a best fit in the simulated spectral region with experimental data characterized for gold dots (Johnson and Christy, 1972). The gold nanodot and its surrounding medium inside the nanodot were divided into meshes 0.5 nm in size.

2.6 AFP detection test with the conventional ELISA

(a) 25 μL of controls (users supplied) and serum samples in duplicate were injected into wells. (b) 100 μL of the incubation buffer was injected into all wells and mixed for 20-30 sec. (c) Then, the wells were incubated for 60 min and washed 3 times with wash buffer. (d) 100 μL of antibody enzyme conjugates were injected into each well. (e) Wells were incubated for 30 minutes and washed 3 times with wash buffer as above. (f) Wells were then dispensed by 100 μL 3,3′,5,5′-tetramethylbenzidine (TMB) substrate and incubated for 15 min. (g) Finally, 50 μL stop solution was injected into each well (the blue color turned to yellow), and the absorbance at 450 nm was measured within 30 min. All procedures were performed at room temperature.

3. Results and Discussion

3.1 Fabrication and characterization of GNA chips

Various techniques have been developed for constructing nano-scaled structures. However, self-assembly methods such as colloidal lithography (Boneberg et al., 1997) and nanosphere lithography (Jensen et al., 2000) do not provide nano-structures with high fidelity over a large area. In addition, direct writing technologies including E-beam lithography (Lin et al., 2010) also suffer from the need for long processing times. In contrast, nanoimprint lithography (NIL) is a suitable approach for fabricating uniform nano-structures over large areas.

In general, thermal and UV methods can be used to transfer a pattern to the substrate in the NIL process. In the thermal method, it is easy to remove the imprinted resin following the imprint and pattern transfer steps. However, in contrast to the UV approach, the thermal method requires long times for substrate heating and cooling as well as high pressure and precise temperature control. As a result, the UV-NIL method was used in this study to

fabricate GNAs on a large wafer. Although an easily UV-curable monomer is often utilized in the UV method, we observed that under these conditions, the polymerized resin could not be readily removed from the substrate using an organic-solvent-promoted lift-off process. To solve this problem, prior to depositing the imprint resin, we introduced a sacrificial layer that could be readily removed using an organic solvent following polymerization. Fig.1b and 1c displays SEM (scanning electron microscope) images of the GNA that are uniformly distributed on a glass wafer. The images show that the GNA has a hexagonal pattern with respective pitch, diameter and height of 300, 150 and 20 nm. This new UV-NIL protocol enabled cost-effective fabrication of mass-producible GNA chips.

The surface plasmon in metal nanostructures resulting in the nanoplasmonic phenomenon is characterized by an electromagnetic field confined near the metal surface. The electromagnetic field induced by incident light is extremely enhanced in close proximity to the surface of the gold nanodots and exponentially decreases in a direction perpendicular to the metal surface. Therefore, the resonance wavelength, extinction amplitude and other characteristics of LSPR are highly sensitive to the environment of the metal nanodots, and, as a result, LSPR can be applied to observe minute changes in the ambient medium brought about by changes in the refractive index.

To evaluate its elementary performance, the LSPR-sensing sensitivity of the fabricated nanodot array was determined using an optical setup with a back-reflection mode. In this mode, light is delivered via an optical fiber to the GNA through the substrate, and the reflected and scattered light from the GNA passes back to the optical fiber along the same pathway. Unlike in the transmission and front-reflection modes, the probe light never passes through the sample solution and, consequently, is not perturbed by temporary inhomogeneity

and turbidity defects in the sample solution. Because using this technique leads to significant suppression of background noise and the coefficient of variation (CV) of the wavelength change, it can be employed to make highly accurate and stable measurements. In addition, the LSPR wavelength is defined as a centroid of the LSP spectrum (λ_{cent}) that can be derived using eq. 1, in which

$$\lambda_{\text{cent}} = \frac{\int_{\lambda_a}^{\lambda_b} \lambda[R(\lambda) - R_B]d\lambda}{\int_{\lambda_a}^{\lambda_b} [R(\lambda) - R_B]d\lambda} \quad (1)$$

$R(\lambda)$ is the experimental reflectance spectrum for LSP as a function of wavelength (λ), R_B is the baseline reflectance value, which was set at 70% of the maximum reflectance in this study, and λ_a and λ_b are the wavelengths of the intersection points of the observed spectrum and the baseline. Instead of using a peak wavelength obtained by polynomial fitting, in this study, a centroid wavelength was utilized as the LSPR wavelength. In this way, the LSPR wavelength is more precisely defined and hence, noise during the measurement is reduced.

Solutions of glycerol at concentrations in the range of 0-40% were employed to evaluate the LSPR wavelength sensitivity of the fabricated GNA, resulting in changes in the refractive index in the range of 1.3329-1.3925 refractive index unit (RIU). Inspection of the spectra displayed in Fig. 2a shows that observable increases in the LSPR wavelength of the GNA take place as the concentration of glycerol and, thus, the refractive index of the solution, increase. The red shift in the LSPR wavelength exhibits an expected linear dependence on the refractive index, and a linear fit of the data (inset plot of Fig. 2a) shows that the sensitivity of the fabricated GNA is 229 nm RIU^{-1}. This sensitivity value is higher than those obtained in

the previous studies using gold nanoparticles, which fall in the range of 50-150 nm RIU^{-1} (Chen et al., 2008; Lin et al., 2010).

As is normally done with conventional nanoparticle-based biosensor systems, the surface of the gold nanodot array was cleaned using piranha solution prior to the immobilization of the antibody. It is found that the sensitivity of the piranha-treated GNA to refractive index changes was 316 nm RIU^{-1} (Fig. 2b). To understand the reason for this 40% increase in sensitivity, the theoretical refractive index sensitivity of the gold nanodot array was calculated using computational electrodynamics that utilized the finite difference time domain (FDTD) method. In this calculation, the background refractive indices were set to those of the solutions that were actually used in the experiments. As can be seen by viewing the calculated spectra and inset plot displayed in Fig. 2c, the results of the calculations show that a linear increase in LSPR wavelength should take place when the concentration of the glycerol solution is increased with a sensitivity value of 219 nm RIU^{-1} for untreated GNA. This value is close to that obtained experimentally (Fig. 2a).

Observations that the calculated and measured sensitivities of the wavelength versus refractive index both change and that differences exist between the experimental sensitivities of piranha-treated and untreated GNA suggest that a topological change in the gold nanodot array occurs upon piranha treatment. To see if this proposal was reasonable, the shapes of piranha-treated and untreated nanodots were determined using transmission electron microscopy (TEM). Thin film-shaped specimens required for TEM measurements were prepared by using cutting, polishing and ion milling (HELIOSNANOLAB by FEI). Fig. 3 shows cross-sections of the gold nanodots on a glass substrate. Inspection of the images reveals that the nanodot is slightly smaller than the original one whose SEM image is shown

in Fig. 1. This discrepancy might be a result of the difficulty incurred when attempting to cut gold a nanodot exactly along its center axis. Inspection of Fig. 3 shows that the titanium layer, located between the gold nanodot and the substrate, is partially etched by the piranha solution treatment. Consequently, the contact area between the titanium layer and the gold nanodot is reduced during the course of piranha treatment, a finding that is in accord with previous observations (Yi et al., 2006).

Generally, gold film does not adhere to a glass surface. As a result, titanium or chromium is used as an under-layer to enhance adhesion. Unfortunately, the use of these transition metal under-layers causes deterioration of the LSPR sensitivities of noble metal nanostructures for the refractive index caused by large optical losses (Habteyes et al., 2012; Hovel et al., 1993; Kreibig et al., 2008; Persson et al., 1993). Therefore, it is likely that the sensitivity increase seen in this effort was caused by partial removal of the titanium during piranha treatment at high temperature (ca. 120 °C). Although the sensitivity improvement caused by reducing the titanium layer is desirable, the mechanical and chemical stability of nanodots on a glass substrate are also reduced. Therefore, to strike a compromise between sensitivity and stability, all GNA chips used in this investigation were treated with piranha solution for 8 min.

Fig. 2d shows the calculated spectra and a plot that gives the theoretical sensitivity for the refractive index of a piranha-solution-treated GNA. It should be noted that an unpolarized white light was used as a probe in the LSPR experiments. To simplify the calculations, however, the incident light employed in the simulations was linearly polarized because the circle-shaped gold nanodots is isotropic to the electric field vector of incident light that vertically impinged on their top surfaces. The calculations took into account the results of the TEM measurements that showed that piranha treatment caused a reduction in the dimensions

of the titanium layer. Utilizing the corrected morphological data on the gold nanodots, the theoretical sensitivity for the treated GNA was found to be 302 nm RIU^{-1}, which was similar to the experimentally determined value (Fig. 2b).

3.2 AFP antigen detection using GNA

Experiments to detect AFP were performed using real-time observation of changes in the LSPR wavelength ($\Delta\lambda$). This approach is advantageous because it enables the reaction between target and receptor molecules to be monitored at each step of the immunoassay and the dynamics of the antigen-antibody interactions to be analyzed. Fig. 4 shows the LSPR spectral changes and the corresponding sensorgrams for several concentrations of AFP. Among the plots, Fig. 4a represents the LSPR spectra of GNA after each stage in the stepwise procedure that was employed to detect 10 ng mL^{-1} of AFP in a human serum. As can be seen, the $\lambda_{cent.}$ of the LSPR band shifted to longer wavelengths during each binding step on the gold nanodot. This behavior, which is typically seen in biosensing experiments that employ LSPR, was a result of the fact that the number of molecules adsorbed on the nanodot surfaces increased, causing a corresponding increase in the refractive index in regions near the nanodot surface. Fig. 4b displays the sensorgram that demonstrates the changes in the LSPR wavelength monitored in real time corresponding to each binding process for Fig. 4a (see also Table S1 of the Supplementary Information). At stage I, immobilization of anti-AFP antibody takes place in association with ca. 4.7 nm red shifts in the LSPR wavelength. The addition of bovine serum albumin to block the nonspecific binding of biomolecules occurs at stage II and brings about a ca. 1.6 nm red shift in the LSPR wavelength. Finally, a ca. 0.9 nm shift occurs in the LSPR wavelength at stage III where AFP antigen binding takes place. The latter wavelength change is the same (ca. 0.3 nm) as that which occurs upon the binding of the

detection antibody (Dab)-enzyme conjugate (stage IV). The small shifts in LSPR wavelength, even when comparatively high concentrations (10 ng mL^{-1}) of the AFP antigen bind and following the addition of the large Dab conjugate, show that it is difficult to detect target molecules in low abundance (sub-ng mL^{-1}) using these experimental conditions (see below). This insensitivity originates from the short penetration depth of the plasmonic field to the ambient media when metal nanostructures and large antibodies are used (Lee et al., 2011).

In order to improve the sensitivity of the LSPR biosensing system, an enzyme-precipitation reaction was conducted (stage V) on the surface of the gold nanodot (nano-ELISA) using a procedure that was described previously (Lee et al., 2011). The enzyme-catalyzed precipitation process causes material to become stacked on the surface, which results in a large increase in the local dielectric constant. The local refractive index jump produces a large shift in the LSPR wavelength (ca. 35 nm).

The atomic force microscope (AFM) images in Fig. 5a show the topological changes in the GNA that take place during the sequential stages, including antibody immobilization, antigen binding and the precipitation reaction. These observations clearly demonstrate that confirmed site-selective accumulation of precipitate occurs around the gold nanodot on the glass substrate after the nano-ELISA process. The theoretical intensity distribution of the local electric field, $|E|^2$, around a gold nanodot was determined by using the FDTD method with back-incidence irradiation at 772 nm employing linearly polarized light through the glass substrate (Fig. 5b). The results of this simulation suggest that the strong plasmonic field, created and mainly distributed at the edges of the gold nanodots (enhancement of ca. 340), is a consequence of the collective oscillation of surface electrons on the metal in response to the electric field associated with the incident light. Fig. 5b shows the average line profiles (B and

C) for the morphology of a single gold nanodot following stages III and V, merged on the distribution map of the electric field intensity induced around a nanodot. These profiles were derived by averaging the height at each position for all observed nanodots in the morphology data field (Fig. S2, Supplementary Information). As can be seen, the antigen molecules were adsorbed mainly on the top surface of the gold nanodot rather than its edge surfaces where the electric field was strong (line B). However, in contrast to the binding of only the antigen, a great number of precipitates produced by the enzyme-catalyzed reaction accumulated on the lateral surfaces as well as the top of the gold nanodot. This phenomenon is likely a crucial factor in eliciting the large increases in the LSPR wavelength.

To investigate the biosensing performance of the GNA chip, studies were performed to detect the AFP antigen quantitatively over a wide concentration range from 1 fg mL^{-1} to 100 ng mL^{-1} (14.28 aM to 14.28 nM)) in human serum. For this purpose, the sandwich immunoassay method depicted in Fig. 4 was utilized and the dependence of changes in the LSPR wavelength ($\Delta\lambda_s$) on the AFP concentration was monitored on the GNA chips (see Table S2 in the Supplementary information). The values correspond to differences in LSPR wavelengths before and after the nano-ELISA reaction on the GNA. As shown in the table, the wavelength change gradually increases with the concentration of the analyte in the whole range of AFP and especially, the increments of $\Delta\lambda_s$ with respect to concentration changes are sufficiently large to enable the quantitative analysis of AFP in the range of 10 pg mL^{-1} to 10 ng mL^{-1}.

However, the differences between the wavelength shifts for each concentration are not sufficiently large when the AFP concentration is reduced below 10 pg mL^{-1} even though their signals are still larger than that of the absolute control (AFP-free serum.) This phenomenon makes it impossible to accurately determine concentrations of AFP below this limit. To lower

the detection limit of the LSPR-based immunoassay, a self-controlled detection scheme was devised. In conventional methods used for this purpose, a separate reference sample containing no analyte needed to be used as a negative control. In the self-controlled scheme, a human serum sample containing a target molecule simultaneously plays the roles of the analyte solution in the sample channel and a negative control in the reference channel. Accordingly, in place of using a separate negative control sample, the portions of the surfaces of gold nanodots, which are not employed as the sample channel, are utilized as a reference channel through passivation (i. e., blocking biochemical interactions) using BSA (Fig. S3). In this way, $\Delta\lambda_c$ is not a consequence of specific antigen-antibody interactions but rather a result of the nonspecific binding of mainly albumin in the serum, which is not dependent on AFP concentration. Thus, the quantitative analysis was carried out by simultaneously measuring changes in the LSPR wavelengths in the sample ($\Delta\lambda_s$) and control ($\Delta\lambda_c$) channels (Table S3). The average value of $\Delta\lambda_c$ was found to be ca. 3.5 nm, and the deviation range of $\Delta\lambda_c$ is non-negligible in comparison with the differences between the $\Delta\lambda_s$ values in the extremely low concentration range. The deviation between $\Delta\lambda_c$ and the differences between $\Delta\lambda_s$ in the sub-pg mL^{-1} concentration region (Table S2, S3) were likely a result of the different amounts of immobilized antibodies on and different levels of nonspecific binding due to different extents of blocking on each GNA chip.

Fig. 6 and the data in Table S4 can be employed to visualize the differences between the sample and control LSPR wavelength shifts ($\Delta\lambda_s$ - $\Delta\lambda_c$) for assays carried out in the AFP concentration range of 1 fg mL^{-1} to 100 ng mL^{-1}, utilizing the label-free detection and enzyme-enhanced sensing schemes. As represented in the plots, the $\Delta\lambda_s$ - $\Delta\lambda_c$ values for the enzyme-enhanced LSPR vary in essentially a sigmoidal manner with AFP concentration over

the nearly entire range. Owing to this finding, it is clear that the data derived from using the self-controlled scheme enable detecting the target at extremely low concentrations. In addition, because deviations from the average values for each concentration are small, it might be possible to determine the amount of target in the samples with using the calibration curve obtained by data fitting with a modified sigmoidal function as shown in Fig.6 (see Table S5 in the supplementary information for the data fitting). Indeed, implementation of the self-controlled scheme described above leads to minimization of the detection inaccuracies that arise from these factors.

3.3 Estimation of LOD

To estimate the LOD in our immunosensing scheme, the experiment was performed for an absolute control, in which an AFP-free human serum was used as the absolute control sample. As shown in Fig. 6, the average value of $\Delta\lambda_s - \Delta\lambda_c$ for the absolute control did not exceed 1 nm. Finally, the LOD was ~1 fg mL^{-1}, which was calculated from the average value and the standard deviation of the data for the absolute control experiment, see Table S4 and 'calculation of LOD' in the Supplementary Information).

The plot of Fig. 6 also compares the sensitivities of assays that employ the nano-ELISA enhanced-LSPR wavelength method with those that do not employ this technique (*i.e.*, only antigen-antibody binding without nano-ELISA). The data show that using the label-free detection procedure, changes in the LSPR shift differences ($\Delta\lambda_s - \Delta\lambda_c$) with variations in the concentrations of AFP are smaller than ±0.5 nm, which is not sufficiently large to enable discrimination of very low concentrations of the target. In contrast, the wavelength shifts at 1 fg mL^{-1} concentration for LSPR detection enhanced using nano-ELISA is similar to that at

100 ng mL^{-1} employing label-free detection. This difference corresponds to a sensitivity enhancement of 10^8.

Finally, to compare the suggested LSPR-based assay that was assisted by nano-ELISA with a conventional immunoassay using ELISA, AFP titrations in the concentration range of 5 ng mL^{-1} to 500 ng mL^{-1} were performed using an ELISA kit (Fig. S4). The LOD in the ELISA assay is 93 pg mL^{-1}, determined using a baseline defined as 3 times the standard deviation of the signals of a negative control along with a calibration curve obtained by fitting with absorbance versus the AFP concentration data. Compared with that of the ELISA assay, the target detection sensitivity of the LSPR measurement, assisted by using nano-ELISA and the self-controlled scheme, is roughly 5 orders of magnitude higher. Consequently, by employing the enhancement from the nano-ELISA method along with the self-controlled scheme for detecting AFP, we were able to detect the AFP antigen in a small volume (50 μL) of human serum at the extremely low concentration of 1fg mL^{-1}, which corresponds to an amount of 714 yoctomol in the sample solution. This detection limit is lower than those of other LSPR-based AFP assays that were reported on previously, most of which were performed in PBS buffer or 50% diluted human serum (Acimovic et al., 2014; Xu et al., 2011) and which fall in the range of 1-20ng mL^{-1} (Liang et al., 2015; Li et al., 2015). Therefore, this study is the first to demonstrate that sub-zeptomolar detection of AFP in undiluted human serum can be accomplished.

4. Conclusions

In the investigation described above, an ultra-sensitive method for detecting biomarkers in human serum was developed. The assay technique used LSPR and a gold nanodot array. The UV-NIL-based procedure used to fabricate the GNA was improved by applying a sacrificial

layer prior to a coating of resin. As a result, the imprinted UV-cured resin was easily removed in the lift-off procedure, giving the GNA high fidelity on a glass substrate. Because it reduces the size of the titanium layer under the gold nanodots, piranha treatment of GNA chips was found to lead to an increase in the sensitivity to detecting refractive index changes. In addition, stable and precise monitoring of LSPR wavelength changes in the assay can be achieved using a back-reflection observation mode in which the probe light never passes through the sample solution. Furthermore, to amplify the changes in wavelength for detecting AFP using LSPR, an enzyme-catalyzed, site-selective precipitation reaction was carried out on the gold nanodots (nano-ELISA) after the antigen and the Dab conjugate were bound. Implementation of this procedure led to a highly enhanced red shift in the LSPR wavelength. Finally, in the assay approach, the new methods described above were employed in conjunction with a self-control detection scheme in which the analyte sample simultaneously served as the target sample in the sample channel functionalized with the specific antibody and as the negative control in the reference channel passivated with BSA. Significantly, the newly designed system enabled detection of extremely small amounts (0.7 zeptomole in 50 μL human serum) of the AFP antigen with a dynamic range spanning 9 orders of magnitude. This system is the first to achieve sub-zeptomole of antigen detection in real serum, which is approximately one hundred thousand times more sensitive than that which can be obtained using a conventional ELISA immunoassay. Moreover, it is anticipated that the performance of the current LSPR detection strategy can be further improved via the novel design of new metal nanostructures for obtaining high-sensitivity LSPR biosensing and low nonspecific binding on metal surfaces. Therefore, it is expected that the LSPR biosensing protocol developed in this effort will serve as a tool for discovering novel disease markers as well as early diagnosis of disease based on molecular detection.

Acknowledgements

This research was financially supported by a grant (NRF-2014R1A2A1A11050768) through the National Research Foundation of Korea (NRF), by BioNano Health-Guard Research Center funded by the Ministry of Science, ICT & Future Planning (MSIP) of Korea as Global Frontier Project (Grant number H-GUARD_2015M3A6B2068406), by the Brain Research Program through the National Research Foundation of Korea (NRF) funded by the Ministry of Science, ICT & Future Planning (2015M3C7A1029113) and by the KRIBB Initiative Research Program (KRIBB, Korea).

Supplementary information

Supplementary data associated with this article can be found in the online version at

References

Acimovic, S. S., Ortega, M. A., Sanz, V., Berthelot, J., Garcia-Cordero, J. L., Renger, J., Maerkl, S. J., Kreuzer, M. P., Quidant, R., 2014. Nano letters. 14, 2636-41.

Boneberg, J., Burmeister, F., Schäfle, C., Leiderer, P., Reim, D., Fery, A., Herminghaus, S., 1997. Langmuir. 13, 7080-7084.

Brown, L. V., Zhao, K., King, N., Sobhani, H., Nordlander, P., Halas, N. J., 2013. Journal of the American Chemical Society. 135, 3688-3695.

Byun, J.-Y., Shin, Y.-B., Li, T., Park, J.-H., Kim, D.-M., Choi, D.-H., Kim, M.-G., 2013. Chemical Communications. 49, 9497-9499.

Chang, Y.-F., Chen, R.-C., Lee, Y.-J., Chao, S.-C., Su, L.-C., Li, Y.-C., Chou, C., 2009. Biosensors and Bioelectronics. 24, 1610-1614.

Chen, H., Kou, X., Yang, Z., Ni, W., Wang, J., 2008. Langmuir. 24, 5233-5237.

Dahlin, A. B., Chen, S., Jonsson, M. P., Gunnarsson, L., Käll, M., Höök, F., 2009. Analytical Chemistry. 81, 6572-6580.

Endo, T., Kerman, K., Nagatani, N., Takamura, Y., Tamiya, E., 2005. Analytical Chemistry. 77, 6976-6984.

Fu, Z., Hao, C., Fei, X., Ju, H., 2006. Journal of Immunological Methods. 312, 61-67.

Geddes, C.D., Cao, H., Gryczynski, I., Gryczynski, Z., Fang, J. Y., Lakowicz, J.R. J., 2003. Phys. Chem. A. 107, 3443-3449

Guo, L., Kim, D.-H., 2012. Biosensors and Bioelectronics. 31, 567-570.

Guo, Z., Hao, T., Wang, S., Gan, N., Li, X., Wei, D., 2012. Electrochemistry Communications. 14, 13-16.

Jeong, H.-H., Lee, S.-K., 2011. J. Sens. Sci. Technol. 20, 107–113.

Ha, T., Enderle, T., Ogletree, D. F., Chemla, D. S., Selvin, P. R., Weiss, S., 1996. Proceedings of the National Academy of Sciences of the United States of America. 93, 6264-6268

Habteyes, T. G., Dhuey, S., Wood, E., Gargas, D., Cabrini, S., Schuck, P. J., Alivisatos, A. P., Leone, S. R., 2012. ACS Nano. 6, 5702-5709.

Haes, A. J., Van Duyne, R. P., 2002. Journal of the American Chemical Society. 124, 10596-10604.

Haes, A. J., Zou, S., Schatz, G. C., Van Duyne, R. P., 2003. The Journal of Physical Chemistry B. 108, 109-116.

Haes, A.J., Duyne, R.P., 2004. Expert Review of Molecular Diagnostics. 4, 527-537.

Haynes, C. L., Yonzon, C. R., Zhang, X., Van Duyne, R. P., 2005. Journal of Raman Spectroscopy. 36, 6-7.

Hovel, H., Fritz, S., Hilger, A., Kreibig, U., Vollmer, M., 1993. Phys. Rev. B. 48, 18178–18188.

J.-H., Bernard, C., Variola, F., Zalzal, S. F., Wuest, J. D., Rosei, F., Nanci, A., 2006. Surface Science. 600, 4613-4621.

Jeanmaire, D. L., Van Duyne, R.P. J., 1977. Electroanal. chem. Interface Electrochem. 84, 1-20.

Jensen, T. R., Malinsky, M. D., Haynes, C. L., Van Duyne, R. P., 2000. The Journal of Physical Chemistry B. 104, 10549-10556.

Johnson, P. B., Christy, R. W., 1972. Phys. Rev. B. 6, 4370-4379.

Jonsson, M. P., Dahlin, A. B., Jönsson, P., Höök, F., 2008. Biointerphases. 3, FD30-FD40.

Kim, H., Jin, S., Lee, S., Kim, M., Shin, Y., 2009. Sensors. 9, 2334–2344.

Kim, M.-G., Shin, Y.-B., Jung, J.-M., Ro, H.-S., Chung, B. H., 2005. Journal of Immunological Methods. 297, 125-132.

Kreibig, U., 2008. Appl. Phys. B: Lasers Opt. 93, 79–89.

Lee, S.-W., Lee, K.-S., Ahn, J., Lee, J.-J., Kim, M.-G., Shin, Y.-B., 2011. ACS nano. 5, 897-904.

Li, W., Jiang, X., Xue, J., Zhou, Z., Zhou, J., 2015. Biosensors and Bioelectronics. 68, 468-474.

Liang, G., Zhao, Z., Wei, Y., Liu, K., Hou, W., Duan, Y., 2015. RSC Advances. 5, 23990-23998.

Lin, Y., Zou, Y., Mo, Y., Guo, J., Lindquist, R. G., 2010. Sensors. 10, 9397-9406.

Liu, X., Wu, H., Zheng, Y., Wu, Z., Jiang, J., Shen, G., Yu, R., 2010. Electroanalysis. 22, 244-250.

Mock, J. J., Smith, D. R., Schultz, S., 2003. Nano letters. 3, 485-491.

Nath, N., Chilkoti, A., 2004. Analytical Chemistry. 76, 5370-5378.

Persson, B. N. J., 1993. Surf. Sci. 281, 153–162.

Raschke, G., Kowarik, S., Franzl, T., Sönnichsen, C., Klar, T. A., Feldmann, J., Nichtl, A., Kürzinger, K., 2003. Nano letters. 3, 935-938.

Schultz, S., Smith, D. R., Mock, J. J., Schultz, D. A., 2000. Proceedings of the National Academy of Sciences. 97, 996-1001.

Seppälä M, Ruoslahti E., 1973. American Journal of Obstetrics and Gynecology. 115, 48-52.

Tsai, W.-C., Lin, I. C., 2005. Sensors and Actuators B: Chemical.106, 455-460.

Touahir, L., Galopin, E., Boukherroub, R., Gouget-Laemmel, A.C., Chazalviel, J.-N., Ozanam, F., Szunerits, S., 2010. Biosensors and Bioelectronics. 25, 2579-2585.

Wang, G.-L., Xu, J.-J., Chen, H.-Y., Fu, S.-Z., 2009. Biosensors and Bioelectronics. 25, 791-796.

Xu, X., Ying, Y., Li, Y., 2011. Procedia Engineering. 25, 67-70.

Yang, J., Moraillon, A., Siriwardena, A., Boukherroub, R., Ozanam, F., Gouget-Laemmel, A.C., Szunerits, S., 2015. Analytical Chemistry. 87, 3721-3728.

Yguerabide, J., Yguerabide, E. E., 1998. Analytical Biochemistry. 262, 137-156.

Yonzon, C. R., Stuart, D. A., Zhang, X., McFarland, A. D., Haynes, C. L., Van Duyne, R. P., 2005. Talanta. 67, 438-448.

Zhu, Q., Ruo, Y., Yaqin, C., Wang, N., Zhuo, Y., Zhang, Y., Li, X.L., 2006. Electrochim. Acta. 51, 3763–3768.

Figure 1 (a) Chip fabrication schematics of the gold nanodot array (GNA) through UV nanoimprint lithography (UV-NIL), (b) SEM image of gold nanodot array (GNA) uniformly fabricated using UV nanoimprint lithography on a substrate and (c) Tilted image of the GNA. The height and diameter of the nanodots are 20 nm and 150 nm, respectively.

Figure 2 Reflectance spectra of LSPR obtained from the GNA at various concentrations of glycerol solution (0-40%). (a) and (b) are experimentally measured spectra from the untreated and piranha-treated GNA, respectively. (c) and (d) are calculated spectra using FDTD simulation for the untreated and piranha-treated conditions, respectively. The inset plot in each spectrum is the linear fit of the LSPR wavelength at the refractive index of each glycerol solution, the slope of which depicts the wavelength versus refractive index sensitivity.

Figure 3 Transmission electron microscope (TEM) image of a gold nanodot; (a) untreated gold nanodot, (b) and (c) piranha-treated for 5 and 10 min, respectively. The yellow arrows indicate the reduction of the Ti layer as the treatment time in the piranha solution increases.

Figure 4 LSPR spectral changes after each step in the immunoassay for AFP concentration (a) 10ng mL^{-1}, (c) 100pg mL^{-1}, (e) 1pg mL^{-1}, (g) 10fg mL^{-1}. (b), (d), (f) and (h) are the real-time sensorgrams for (a), (c), (e) and (g), respectively. The inset graphs of each spectrum depict the values of the LSPR wavelength measured after each step.

Figure 5 (a) AFM images of the GNA obtained after each binding step; the immobilization of anti-AFP antibody on GNA surface (A), the binding of 10 ng mL^{-1} AFP with anti-AFP antibody on the GNA (B), and the precipitate reaction on the surface (C). (b) Intensity distribution of the calculated electric field around a gold nanodot on top of a glass substrate (n = 1.52), $|E|^2$ at 772 nm wavelength by FDTD. The surrounding medium is water (n = 1.33), and the wave vectors k and E represent the incident direction of the probe light and the polarization direction, respectively. In (b), the dotted lines depict the averaged line profiles of the gold nanodot after antigen binding (B) and the precipitate reactions (C), which are obtained from the AFM measurement (a).

Figure 6 Dependence of the differences ($\Delta\lambda_s$ - $\Delta\lambda_c$) between the sample and control data in AFP concentration for label-free detection (blue circle) and enzyme-enhanced sensing (nano-ELISA, red circle). All experiments were repeated 3 times, and the error bars represent the standard deviations of the LSPR wavelength shifts according to each concentration. The red and blue lines depict the calibration curves obtained from data fitting with a sigmoidal function for each detection scheme. The red dashed line represents the limit of detection, which corresponds to the sum of the average wavelength shift and 3 times the standard deviation for the absolute control (the human serum without AFP) in the enhanced LSPR experiment.

Highlights

- Gold nanodot array was fabricated on a 5-inch glass wafer using UV nanoimprint.
- Localized surface plasmon-based biosensor was realized with back reflection mode.
- AFP in human serum was detected with range from 10 fg mL^{-1} to 10 ng mL^{-1}

- Ultra-sensitive detection of biomarker could be achieved by self-controlled scheme.

Figure 1.

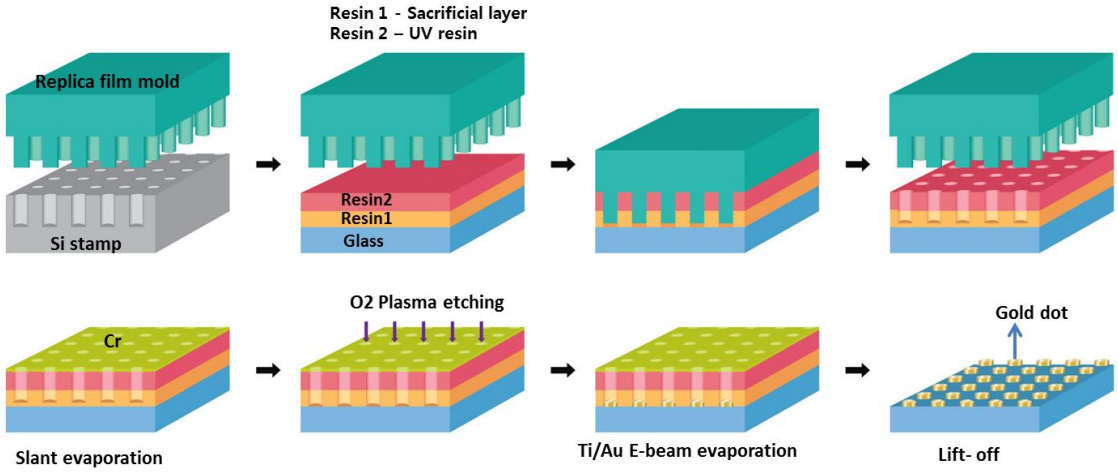
Resin 1 - Sacrificial layer
Resin 2 – UV resin
Replica film mold
Si stamp
Resin2
Resin1
Glass
Cr
O2 Plasma etching
Gold dot
Slant evaporation
Ti/Au E-beam evaporation
Lift- off

(a)

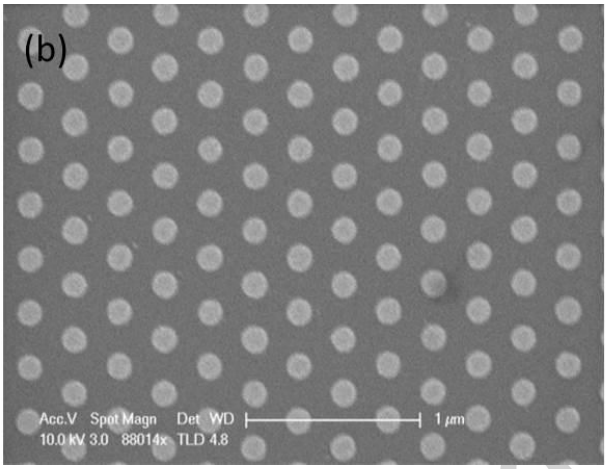
(b)
Acc.V Spot Magn Det WD 1 μm
10.0 kV 3.0 88014x TLD 4.8

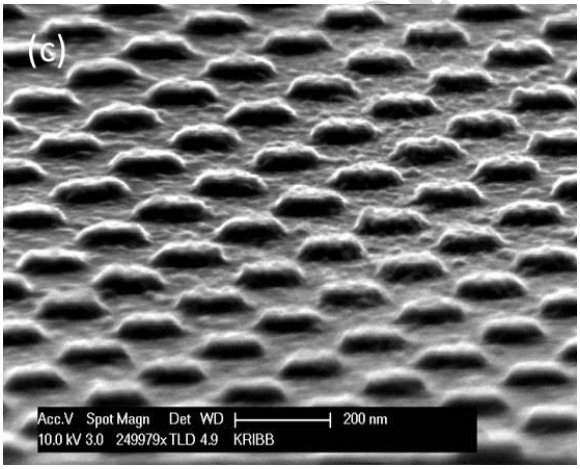
(c)
Acc.V Spot Magn Det WD 200 nm
10.0 kV 3.0 249979x TLD 4.9 KRIBB

Figure 2.

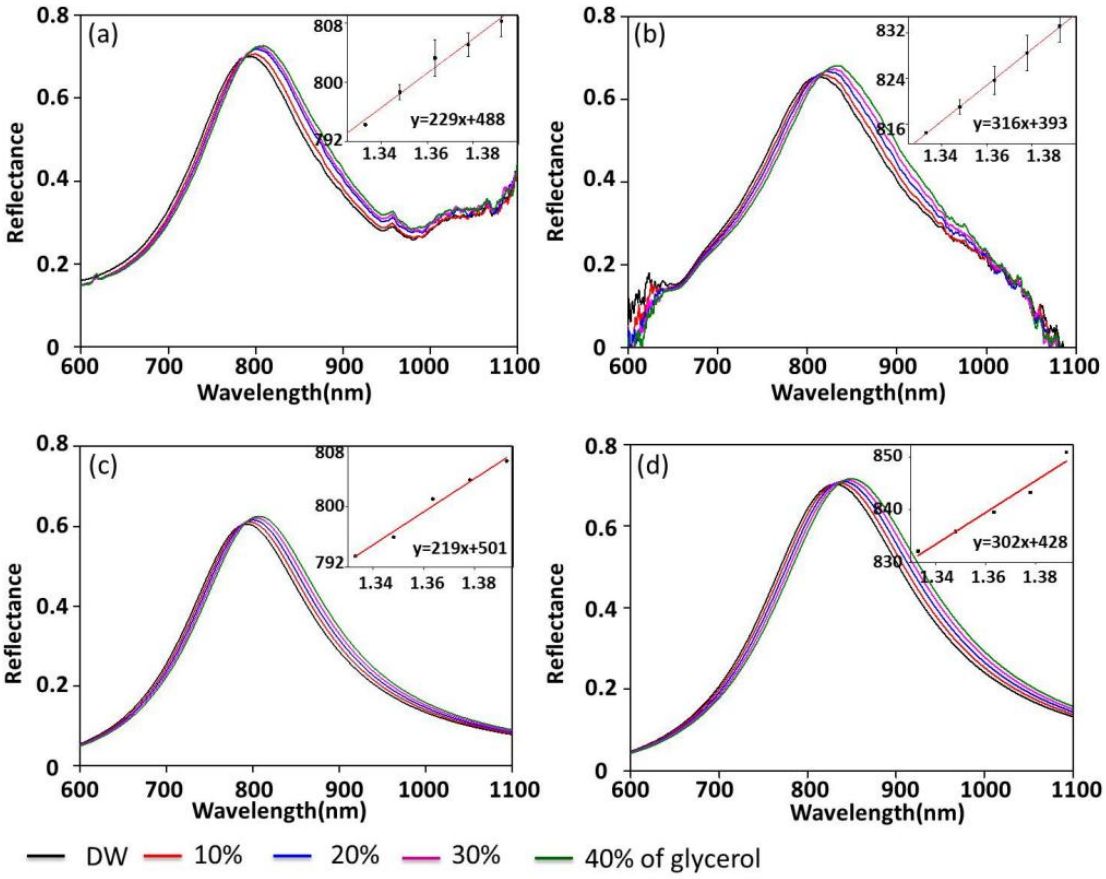

Figure 3.

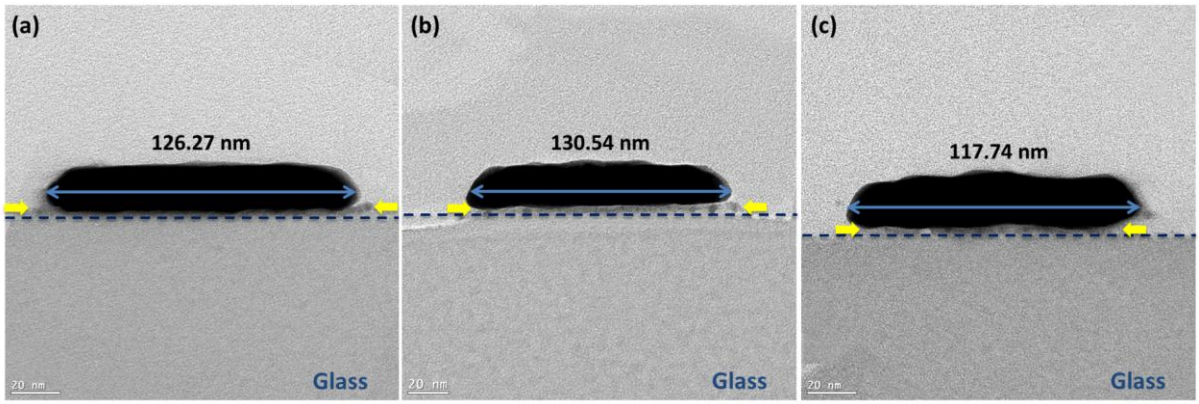

Figure 4.

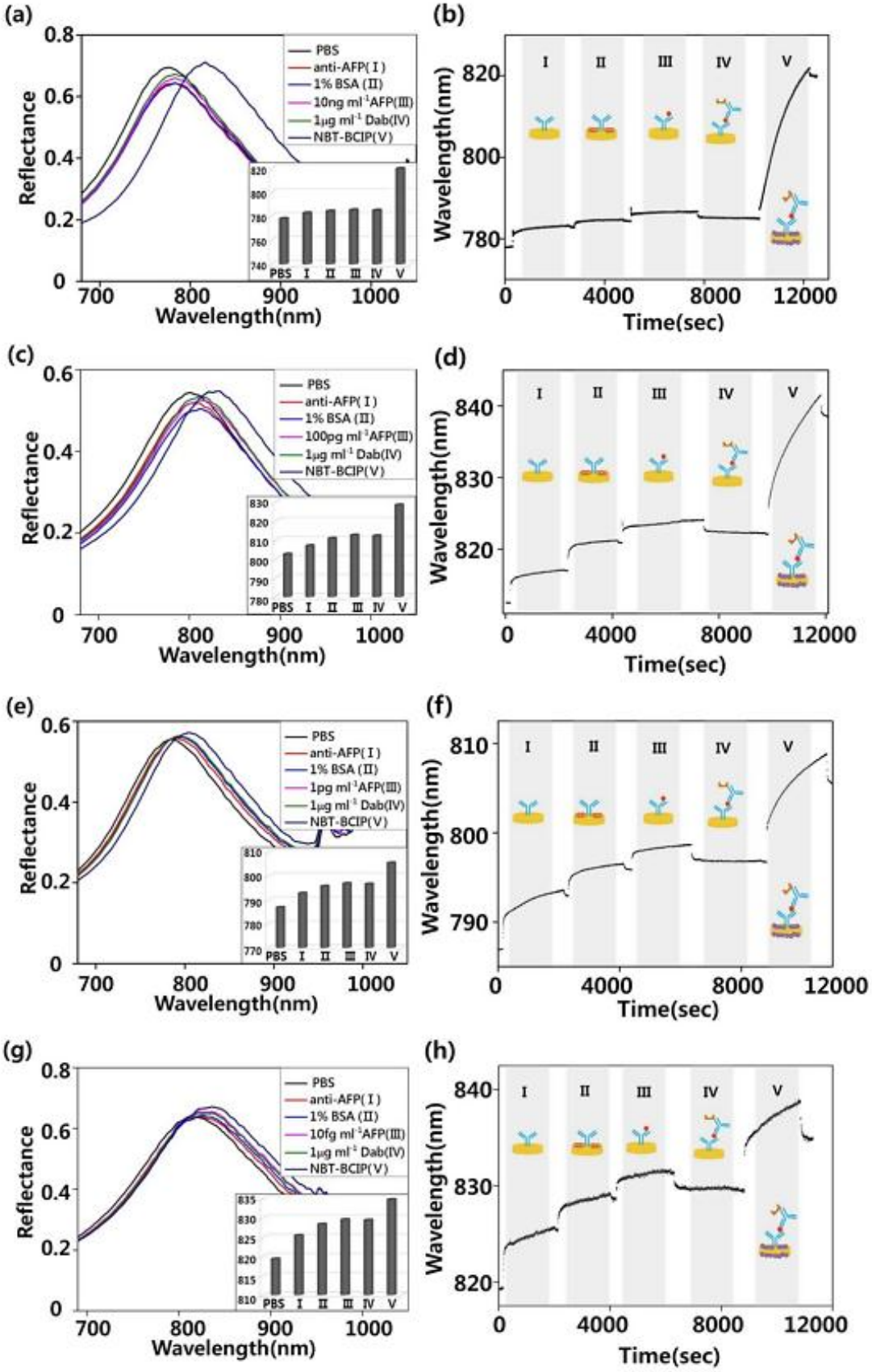
(a)
Reflectance
Wavelength(nm)
PBS
anti-AFP(Ⅰ)
1% BSA (Ⅱ)
10ng ml⁻¹AFP(Ⅲ)
1μg ml⁻¹ Dab(Ⅳ)
NBT-BCIP(Ⅴ)
PBS Ⅰ Ⅱ Ⅲ Ⅳ Ⅴ
(b)
Wavelength(nm)
Time(sec)
Ⅰ Ⅱ Ⅲ Ⅳ Ⅴ
(c)
Reflectance
Wavelength(nm)
PBS
anti-AFP(Ⅰ)
1% BSA (Ⅱ)
100pg ml⁻¹AFP(Ⅲ)
1μg ml⁻¹ Dab(Ⅳ)
NBT-BCIP(Ⅴ)
(d)
Wavelength(nm)
Time(sec)
(e)
Reflectance
Wavelength(nm)
PBS
anti-AFP(Ⅰ)
1% BSA (Ⅱ)
1pg ml⁻¹AFP(Ⅲ)
1μg ml⁻¹ Dab(Ⅳ)
NBT-BCIP(Ⅴ)
(f)
Wavelength(nm)
Time(sec)
(g)
Reflectance
Wavelength(nm)
PBS
anti-AFP(Ⅰ)
1% BSA (Ⅱ)
10fg ml⁻¹AFP(Ⅲ)
1μg ml⁻¹ Dab(Ⅳ)
NBT-BCIP(Ⅴ)
(h)
Wavelength(nm)
Time(sec)

Figure 5.

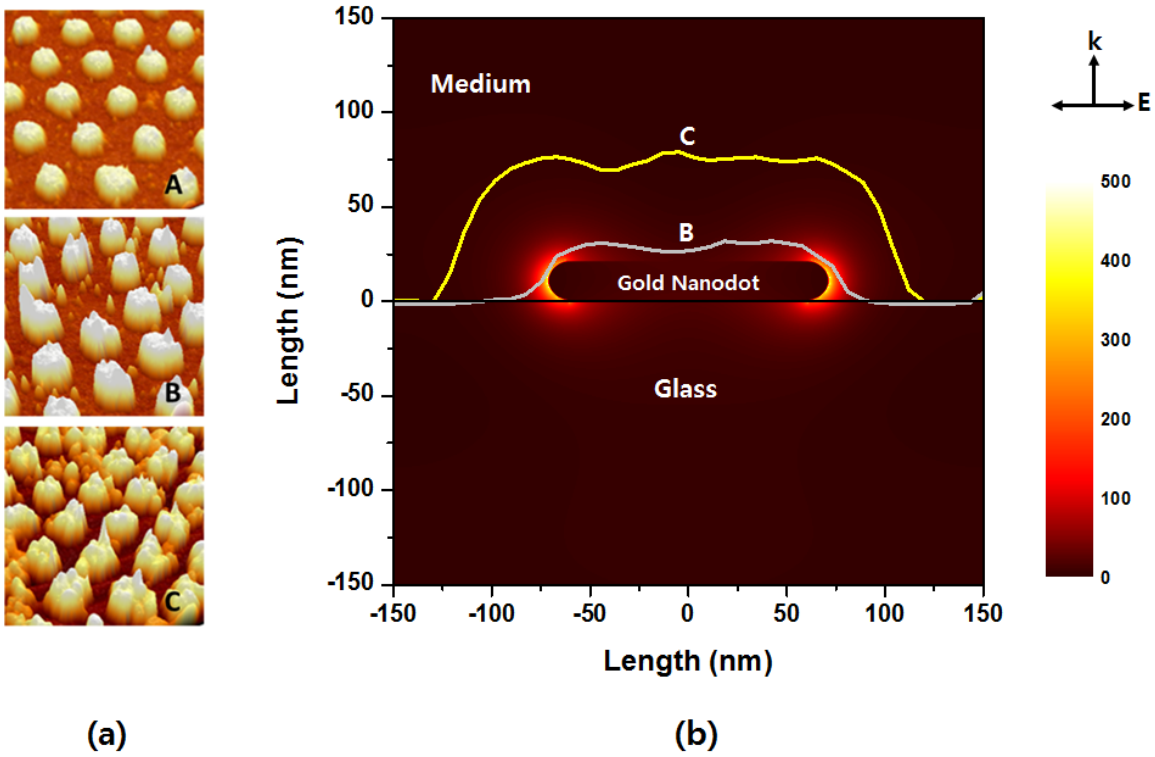

(a) (b)

Figure 6